ADVANCES IN ATMOSPHERIC SCIENCES, VOL. 34, MAY 2017, 635–649

• **Original Paper** •

Changes in Surface Energy Partitioning in China over the Past Three Decades

Yitian QIAN[1], Pang-Chi HSU*[1], and Chi-Han CHENG[2]

[1]*Key Laboratory of Meteorological Disaster of Ministry of Education/Joint International Research Laboratory of Climate and Environment Change/Collaborative Innovation Center on Forecast and Evaluation of Meteorological Disasters, Nanjing University of Information Science and Technology, Nanjing, Jiangsu* 210044*, China*

[2]*Applied Hydrometeorological Research Institute, Nanjing University of Information Science and Technology, Nanjing, Jiangsu* 210044*, China*

(Received 25 July 2016; revised 4 November 2016; accepted 24 November 2016)

ABSTRACT

Surface energy balance and the partitioning of sensible heat flux (SHF) and latent heat flux (LHF) play key roles in land–atmosphere feedback. However, the lack of long-term observations of surface energy fluxes, not to mention spatially extensive ones, limits our understanding of how the surface energy distribution has responded to a warming climate over recent decades (1979–2009) at the national scale in China. Using four state-of-the-art reanalysis products with long-term surface energy outputs, we identified robust changes in surface energy partitioning, defined by the Bowen ratio (BR = SHF/LHF), over different climate regimes in China. Over the past three decades, the net radiation showed an increasing trend over almost the whole of China. The increase in available radiative energy flux, however, was balanced by differential partitioning of surface turbulent fluxes, determined by local hydrological conditions. In semi-arid areas, such as Northeast China, the radiative energy was transferred largely into SHF. A severe deficiency in near-surface and soil moistures led to a significant decreasing trend in LHF. The combined effect of increased SHF and decreased LHF resulted in significant upward trends in the BR and surface warming over Northeast China. In contrast, in the wet monsoon regions, such as southern China, increased downward net radiation favored a rise in LHF rather than in SHF, leading to a significant decreasing trend in the BR. Meanwhile, the increased LHF partly cancelled out the surface warming. The warming trend in southern China was smaller than that in Northeast China. In addition to impacts on heat-related events, the changes in the BR also reflected recent cases of extreme drought in China. Our results indicate that information regarding the BR may be valuable for drought monitoring, especially in regions prone to such conditions.

Key words: surface energy partitioning, Bowen ratio, climate change, long-term trend

Citation: Qian, Y. T., P.-C. Hsu, and C.-H. Cheng, 2017: Changes in surface energy partitioning in China over the past three decades. *Adv. Atmos. Sci.*, **34**(5), 635–649, doi: 10.1007/s00376-016-6194-8.

1. Introduction

The surface energy budget includes both radiative (solar radiation and longwave radiation) and non-radiative (sensible, latent, and ground heat fluxes) components. Increased net radiation (NR, downwards minus upwards) is mostly balanced by the turbulent processes of sensible heat flux (SHF) and latent heat flux (LHF) from the surface towards the atmosphere. Through the exchanges of energy and momentum across the planetary boundary layer, the processes related to surface energy balance modify the structure of the overlying atmosphere and exert influences on local climate, as well as hydrological and biogeochemical cycling (e.g., Shukla and Mintz, 1982; Collatz et al., 2000; Bounoua et al., 2002; Chapin et al., 2002; Defries et al., 2002; Chen et al., 2003). Subsequently, these atmospheric and hydrological changes affect solar and longwave radiation through cloud–radiation feedback (Boer, 1993). Therefore, surface energy balance and the partitioning between turbulent fluxes (SHF/LHF) are a critical part of land–atmosphere feedback, and closely related to climate variability.

Changes in solar radiation associated with global dimming and brightening have received much attention (Liepert, 2002; Wild et al., 2004, 2005). A reduction in downward solar radiation from the 1960s to the 1980s was confirmed at several radiation stations around the world (Stanhill and Cohen, 2001; Liepert, 2002). The decreasing trend in solar radiation levelled off around 1990; and after that, a rising trend in surface solar radiation was reported through both satellite and surface observations (Wild et al., 2004, 2005; Pinker et al., 2005). Compared to this long-term variation in solar radiation, analyses of turbulent energy fluxes have been somewhat limited, due to the difficulty and high cost of eddy-covariance

* Corresponding author: Pang-Chi HSU
Email: pangchi@nuist.edu.cn

measurements. Nevertheless, based on one year of data in the Florida Everglades, Schedlbauer et al. (2011) investigated the seasonality of surface energy fluxes and found that SHF was principally dominant in the dry season, and LHF in the wet season. Earlier, Tanaka et al. (2001) used the observations from GEWEX (Global Energy and Water Cycle Experiment) at a planetary boundary layer tower site on the Tibetan Plateau to understand the differences in surface energy balance between pre-monsoon and monsoon seasons. They indicated that SHF was dominant in the pre-monsoon season, due to a relatively dry surface; whereas, during the monsoon season when precipitation is abundant, SHF started to decrease but LHF increased. Using long-term (2003–12) surface energy observational data at a subtropical plantation site in Southeast China, Tang et al. (2014) documented that the reduction in the Bowen ratio (BR = SHF/LHF) over the period 2003–12 was closely linked to increased rainfall frequency. These studies help to highlight the influences of the seasonal climate condition on surface energy partitioning.

But how does surface energy partitioning (or the BR) respond to climate change? Keenan et al. (2013) analyzed energy fluxes at 21 forest sites with records ranging from 7 to 18 years. The results showed that, due to the adjustment of leaf stomata, an increasing trend of the BR appeared to accompany increasing carbon dioxide. However, the results of Lamarque et al. (2013) and Richardson et al. (2013) suggested that the BR tends to decline under a warmer climate, because the increased energy induced by increased carbon dioxide is consumed as LHF rather than as SHF. Thus, understanding how surface energy partitioning changes under global warming, and the associated climate impacts, is an important issue for countries vulnerable to meteorological disasters, such as China. However, such a topic is challenging and rarely tackled, not least because of the spatial limitation (i.e., inhomogeneity) and temporal restriction (i.e., short history) of surface measurements. Recently, a number of studies have assessed surface energy fluxes in reanalysis datasets, concluding reasonable accuracy and reliability when compared to observational measurements (Bosilovich et al., 2011; Jiménez et al., 2011). Thus, there is some potential to investigate long-term changes in surface energy balance and partitioning at regional or global scales by applying these datasets (Shi and Liang, 2014).

The main aim of the present study was to understand the changes in surface energy partitioning over recent decades and their impacts on regional temperature extremes and drought events over different climate regimes (such as arid, semi-arid and humid areas) in China, based on state-of-the-art reanalysis products and meteorological station measurements. The datasets and statistical methods used in the study are introduced in sections 2.1 and 2.2, respectively. To provide confidence in using these reanalysis products, we compared the temporal and spatial characteristics of surface energy fluxes in the reanalysis data against ground-level eddy-covariance measurements, radiation-site observations and satellite-based data. The results of our reanalysis evaluation are presented in section 3. Using the reanalysis products, we present the results regarding surface energy distributions over China and their changes during the past three decades in section 4. The influence of surface energy partitioning on heat and hydrological cycles, and its implications for drought monitoring, are then discussed. Finally, a summary of our key findings is provided in section 5.

2. Datasets and methodology

2.1. *Datasets*

2.1.1. *Reanalysis products*

Four state-of-the-art global reanalysis datasets from different research institutes were collected. Several improvements in data assimilation systems, model parameterizations and resolutions were implemented into these new reanalysis projects. The basic information is summarized below and in Table 1.

The Climate Forecast System Reanalysis (CFSR) is the latest generation NCEP (National Centers for Environmental Prediction) reanalysis product. Different from other reanalyses, in which the first guess fields in the assimilation cycle are from an atmosphere-only model forced by sea surface temperature, CFSR uses its first guess fields from a fully coupled atmosphere–ocean–land-surface–sea-ice model at a high spatial resolution (~38 km). The land data assimilation system in CFSR (GLDAS) is a semi-coupled system that runs the Noah land surface model (Ek et al., 2003) using rain gauge and satellite-based precipitation. The dataset can be download from https://www.ncdc.noaa.gov/data-access/model-data/model-datasets/climate-forecast-system-version2-cfsv2#CFS Reanalysis (CFSR).

ERA-Interim (Dee et al., 2011) is the latest global atmospheric reanalysis produced by the European Centre for Medium-Range Weather Forecasts (ECMWF). The land surface component is based on the TESSEL scheme (Viterbo and Beljaars, 1995). ERA-Interim uses a 12-hourly four-

Table 1. Information on the reanalysis datasets used in this study.

	CFSR	MERRA	ERAI	JRA-55
Agency	NCEP	NASA	ECMWF	JMA
Period	1979–2011	1979–present	1979–present	1958–2014
Horizontal resolution	T382 (~38 km)	0.5(lat)° × 0.66° (lon) (~65 km)	T255 (~79 km)	T319 (~55 km)
Land surface model	Noah land surface model	Catchment land model	TESSEL land model	Offline SiB
Assimilation method	3DVar	3DVar (GEOS-5)	4DVar	4DVar

dimensional variational (4DVar) rather than the 3DVar data assimilation system used in the previous product, ERA-40, and can be downloaded from the ECMWF website at http://apps.ecmwf.int/datasets/.

JRA-55 (Kobayashi et al., 2015), covering 55 years starting from 1958, was developed by the second Japanese global atmospheric reanalysis project of the Japan Meteorological Agency (JMA). It uses the latest JMA operational numerical weather prediction system with the offline SiB land surface scheme. Compared to JRA-25 (the previous JMA reanalysis product), JRA-55 is based on a new 4DVar assimilation system with variational bias correction for satellite radiance and an increased model resolution from T106L40 to TL319L60. The dataset is available at http://jra.kishou.go.jp/JRA-55/index_en.html.

The Modern Era-Retrospective Analysis for Research and Applications (MERRA) is NASA's reanalysis for the satellite era, using the Goddard Earth Observing System atmospheric model, version 5.2.0 (GEOS-5) and data assimilation system. The MERRA GEOS-5 data assimilation system uses 3DVar and an incremental analysis update procedure to slowly adjust the model towards the observation (Rienecker et al., 2011). Land surface processes are modeled by the state-of-the-art GEOS-5 catchment hydrology land surface model. The dataset can be download from https://gmao.gsfc.nasa.gov/reanalysis/MERRA/.

Monthly NR, SHF and LHF during 1979–2009 were collected from the four reanalysis datasets. The four components of NR (downward longwave/shortwave radiation and upward longwave/shortwave radiation) were available in the CFSR, ERA-Interim and JRA-55 datasets. In this study, radiative flux is positive downwards, while turbulent fluxes are positive upwards.

2.1.2. *Observations used for reanalysis validation*

To ensure the quality and reliability of the reanalysis products, the features of surface energy fluxes were compared against the ground-level eddy-covariance measurements from ChinaFLUX, and against the radiation observations from radiation stations and satellites.

ChinaFLUX is an observation and research network that applies eddy covariance of micrometeorology to provide continuous measurements of the exchanges of energy, water and carbon dioxide between land and atmosphere in China. The surface energy fluxes, including NR, SHF and LHF, every 30 minutes from 2003 to 2005, are downloaded from the ChinaFLUX website at http://159.226.111.42/pingtai/LoginRe/opendata.jsp. Considering their geographical locations with different climate states, topography and diverse vegetation types, as well as the data quality (extensive records with small quantities of missing data), we used the surface energy flux measurements from eight sites (Table 2). Among the eight sites, four of them (CBS, HBS, QYZ, and YCS) included all measurement types, i.e., of NR, SHF and LHF, while the other four sites (BNS, DHS, DXS, and NMG) only measured SHF and LHF.

Observational NR data in China can be download from the China Meteorological Data Sharing Service (http://cdc.nmic.cn/home.do). In this study, we collected monthly radiation records from 40 radiation sites with long and complete data records from January 1993 to February 2015.

The Clouds and the Earth's Radiant Energy System (CERES; Wielicki et al., 1996) experiment comprises satellite instruments developed for NASA's Earth Observing System. It was designed to measure the solar-reflected and Earth-emitted radiation from the top of the atmosphere to Earth's surface. The data cover the period from March 2000 to October 2005 and can be download from website at https://ceres.larc.nasa.gov/order_data.php.

2.1.3. *Other meteorological observations*

Considering data uncertainty, we collected daily air temperature and precipitation from three gauge-based datasets to investigate the relationship between changes in surface energy partitioning and atmospheric heat and drought features. The first dataset was the newly released CN05.1 dataset (Wu and Gao, 2013) from the National Climate Center (NCC) in China. This dataset was derived from over 2400 daily station reports in China. The others two were the Asian Precipitation Highly Resolved Observational Data Integration Towards Evaluation of Water Resources (APHRODITE; Yatagai et al., 2012, http://www.chikyu.ac.jp/precip/english/products.html) and the Climatic Research Unit's Global Climate Dataset (Mitchell and Jones, 2005, http://catalogue.ceda.ac.uk/uuid/

Table 2. Information on the ChinaFLUX data used in this study.

	Location	Climate	Vegetation type
Xishuangbanna (BNS)	22°N, 101°E	Tropical monsoon region	Tropical rain forest
Changbaishan (CBS)	42°N, 128°E	Warm and semi-humid monsoon region	Pinus koraiensis broad-leaved mixed forest
Dinghushan (DHS)	23°N, 112°E	Subtropical monsoon humid climate region	Evergreen broad-leaved forest
Dangxiong (DXS)	30°N, 91°E	Plateau monsoon climate region	Alpine meadow area
Haibei (HBS)	38°N, 101°E	Highland continental climate region	Typical frigid vegetation of Northern Qinghai-Tibetan Plateau
Inner Mongolia (NMG)	44°N, 117°E	Continental temperate semi-arid grassland climate region	Leymus chinensis grassland
Qianyanzhou (QYZ)	26°N, 115°E	Subtropical monsoon climate region	Human-planted forest
Yucheng (YCS)	36°N, 116°E	Continental climate region	Wheat in winter and corn in summer

ac4ecbd554d0dd52a9b575d9666dc42d). All three have a horizontal resolution of 0.5°.

Drought conditions in China could be identified quantitatively based on precipitation and temperature observations. The drought composite index (CI; Zou and Zhang, 2008), proposed by the NCC of China, combines the information of the standardized precipitation index (SPI; McKee et al., 1993) and relative moisture index (MI; Zhang et al., 2006):

$$\mathrm{CI} = aZ_{30} + bZ_{90} + cM_{30} \,, \tag{1}$$

where Z_{30} and Z_{90} indicate the 30 and 90-day-mean SPI, respectively, and M_{30} represents the 30-day-mean MI [MI = $(P - \mathrm{Pe})/\mathrm{Pe}$], related to the difference between precipitation (P) and evaporation (Pe) in the past 30 days. The coefficients a, b and c are defined empirically as 0.4, 0.4 and 0.8, respectively. In general, the CI value is negative when a drought occurs. The CI value decreases when drought severity increases.

To consider long-lasting drought events, the staff at the NCC recently developed the comprehensive meteorological drought index (MCI)—an improved version of the CI. The MCI uses the SPI in early stages (previous 90 and 150 days) and further includes an e-folding weighted rainfall in the previous 60 days:

$$\mathrm{MCI} = aZ_{\mathrm{w60}} + bM_{30} + cZ_{90} + dZ_{150} \,, \tag{2}$$

in which Z_{90} and Z_{150} are the 90- and 150-day-mean SPI, M_{30} is the 30-day-mean MI, and Z_{w60} is the 60-day-mean standardized and weighted precipitation index. The coefficients a, b, c and d are defined as 0.3, 0.6, 0.2 and 0.3, respectively. The weighted coefficient for daily precipitation in the past 60 days (Z_{w60}) can be obtained using the following equation:

$$W_k = (1-a)a^k \,, \tag{3}$$

where k is the number of days before each given day, and a is set to 0.9.

2.2. *Statistical methods*

Linear regression analysis was applied to obtain the slope of the trend. To assess if the trend identified was statistically significant, the Mann–Kendall trend test (Mann, 1945; Kendall, 1975), which has been widely used for detecting significant trends in time series, was applied throughout the study. Although parametric trend tests (such as the Student's t-test) are powerful, they require the data to be normally distributed. Different from parametric tests, the non-parametric Mann–Kendall trend test, based on the ranking of data rather than their actual values, allows the data to follow any distribution. Another advantage of the Mann–Kendall trend test lies in its low sensitivity to outliers.

The computational procedure for the Mann–Kendall trend test is described as follows. Given a time series of variable $x(t)$ with duration n, the null hypothesis of no trend assumes that $x(t)$ is independent and identically distributed. Each data value is compared with all subsequent data values, defined as the Mann–Kendall statistic, S:

$$S = \sum_{i=1}^{n-1} \sum_{j=i+1}^{n} \mathrm{sgn}(x_j - x_i) \,, \tag{4}$$

$$\mathrm{sgn}(x_j - x_i) = \begin{cases} 1, x_j - x_i < 0 \\ 0, x_j - x_i = 0 \\ -1, x_j - x_i > 0 \end{cases} \,, \tag{5}$$

where x_j and x_i are the data points at time j and i ($j > i$), respectively. Thus, a positive (negative) value of S indicates an upward (downward) trend. The variance of S, $\mathrm{VAR}(S)$, is calculated by the following equation:

$$\mathrm{VAR}(S) = \frac{n(n-1)(2n+5)}{18} \,. \tag{6}$$

Then, the standard test statistic Z_{c} is defined as

$$Z_{\mathrm{c}} = \begin{cases} \dfrac{S-1}{\sqrt{\mathrm{VAR}(S)}}, & S > 0 \\ 0, & S = 0 \\ \dfrac{S+1}{\sqrt{\mathrm{VAR}(S)}}, & S < 0 \end{cases} \,. \tag{7}$$

If $Z_{\mathrm{c}} > 1.65$ ($Z_{\mathrm{c}} > 1.96$), the null hypothesis is invalid and the trend is statistically significant at the 90% (95%) level.

3. Validation of the reanalysis datasets

The surface energy fluxes in the four reanalysis datasets were compared against the measurements from the ChinaFLUX network at eight locations, each with different topography, climate and surface vegetation (Table 2). Figure 1 displays the time series of monthly NR (Figs. 1q–t), SHF (Figs. 1a–h) and LHF (Figs. 1i–p) during the observational period of 2003–05. Overall, the amplitude and temporal variation of NR (bottom panels) in the four reanalyses were highly consistent, and they also agreed well with the ChinaFLUX observations. The time series of surface turbulent fluxes, however, showed diverse distributions among the reanalysis datasets. This uncertainty may be related to the land surface parameterizations utilized in different reanalysis projects. It is interesting to note that the ensemble of reanalysis outputs could largely reduce the uncertainty of magnitude. At most sites, except for HBS (Figs. 1e and m) in western China and DXS (Fig. 1l) of the Tibetan Plateau, where the reanalysis tended to underestimate SHF and LHF, the ensemble results (red curves) were close to the observations (black curves).

The Taylor diagram (Fig. 2) shows the temporal correlation coefficients (TCCs) and amplitude errors (normalized root-mean-square error, NRMSE) calculated from the ensemble average of the four reanalysis datasets relative to the ChinaFLUX data at the eight sites. Surface NR from the reanalysis data showed very high correlation (TCCs all above 0.96) with observations. The NRMSEs of NR ranged from 0.88 (QYZ) to 1.32 (CBS). The LHF and SHF from the reanalysis data also showed reasonable TCCs (0.6–0.99), but

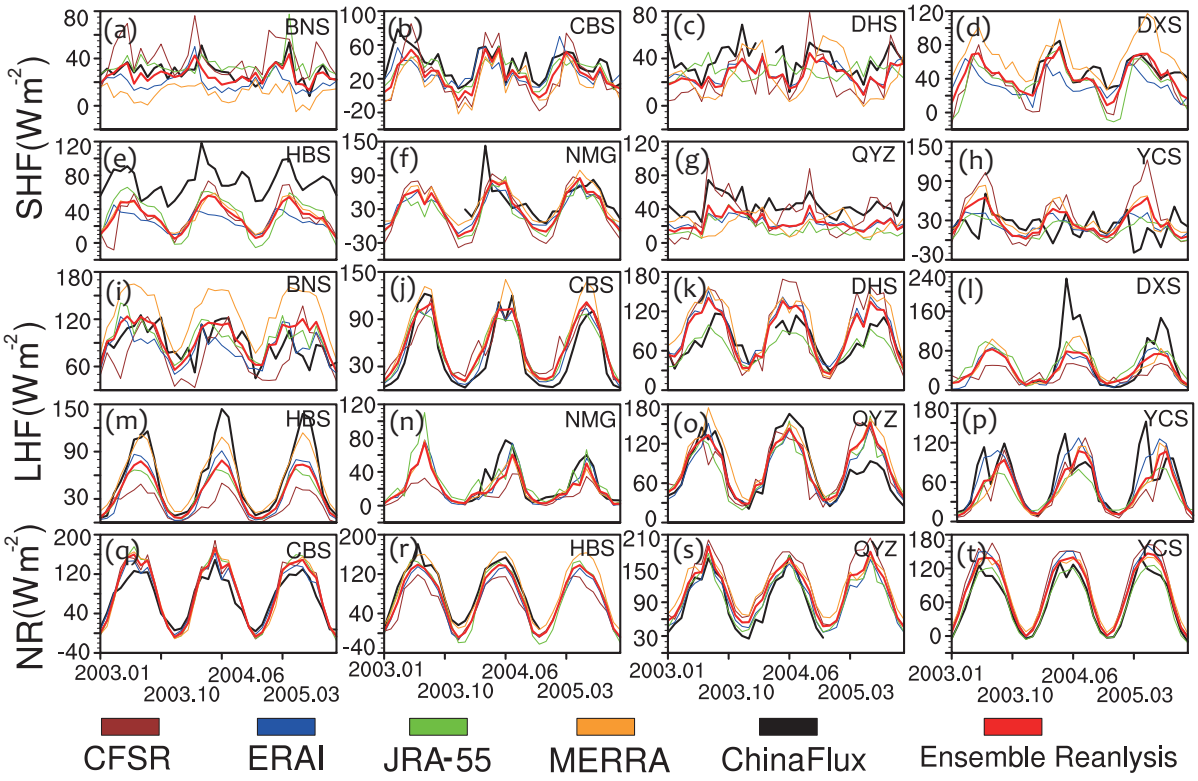

Fig. 1. Comparison of monthly SHF between reanalysis datasets and ChinaFLUX at (a) BNS, (b) CBS, (c) DHS, (d) DXS, (e) HBS, (f) NMG , (g) QYZ and (h) YCS, for the period 2003–2005. The ChinaFlux measurements are shown in black. The reanalysis data from CFSR, ERA-Interim (ERAI), MERRA, and JRA-55 are represented in brown, blue, green and yellow, respectively. Red indicates the ensemble average of the four reanalysis datasets. Units: W m^{-2}. Panels (i–p) are the same as (a–h), except for monthly LHF. Panels (q–t) are a comparison of monthly net radiation for CBS, HBS, QYZ and YCS, respectively.

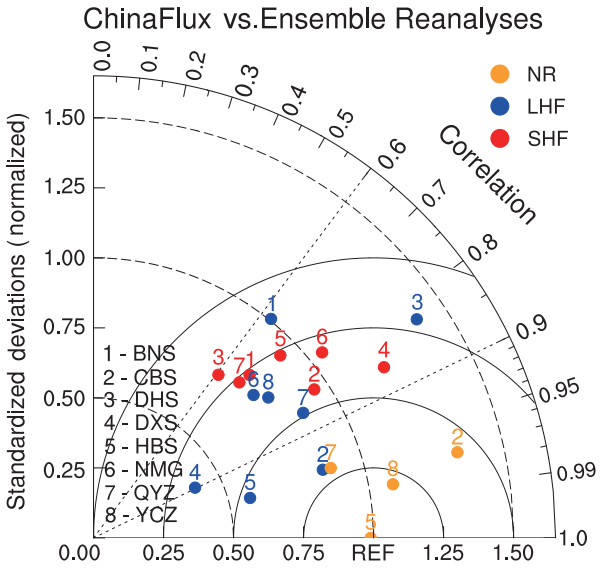

Fig. 2. Taylor diagram for the ensemble of the four reanalyses compared to ChinaFLUX observations of net radiation (yellow), SHF (red) and LHF (blue), at the eight sites (1: BNS, 2: CBS, 3: DHS, 4: DXS, 5: HBS, 6: NMG, 7: QYZ, and 8:YCS) during 2003–05. In the Taylor diagram, normalized standard deviation is on the radial axis, temporal correlation coefficient is on the angular axis, and solid lines indicate normalized root-mean-square error.

with a wide distribution for NRMSEs (0.4–1.4). Large biases [NRMSE (1.03) and TCC (−0.09)] appeared in SHF at YCS (not shown in Fig. 2). We are unsure if the low correlation coefficient between reanalysis and observation was due to the uncertainty in the land models used in the reanalysis, because the SHF variations shown in the four reanalysis datasets revealed high consistency at YCS. Furthermore, these reanalyses captured the SHF variability well, with correlation coefficients of 0.6–0.9 at the other seven locations, confirming the capability of the reanalysis land models. Thus, we argue that the SHF measurement at YCS might be problematic given that eddy-covariance measurements can sometimes be degraded by instrument-related factors and biophysical conditions (Yu et al., 2006; Liu et al., 2009).

Because of the limited number of ChinaFLUX sites, their capability to capture the spatial distribution of radiative flux was validated by calculating the TCCs between the reanalysis data and satellite-based observations (Fig. 3). High TCCs (> 0.95) were found for all the reanalysis products over almost the whole of China, except over southern China where relatively low TCCs (0.75–0.9) were observed. Even so, the TCCs all exceeded the 99% significance level. Similar results were found for the TCCs of the reanalysis data with observations from radiation stations in China (Fig. 4). TCCs beyond 0.95 were observed in North and Northeast China. Although

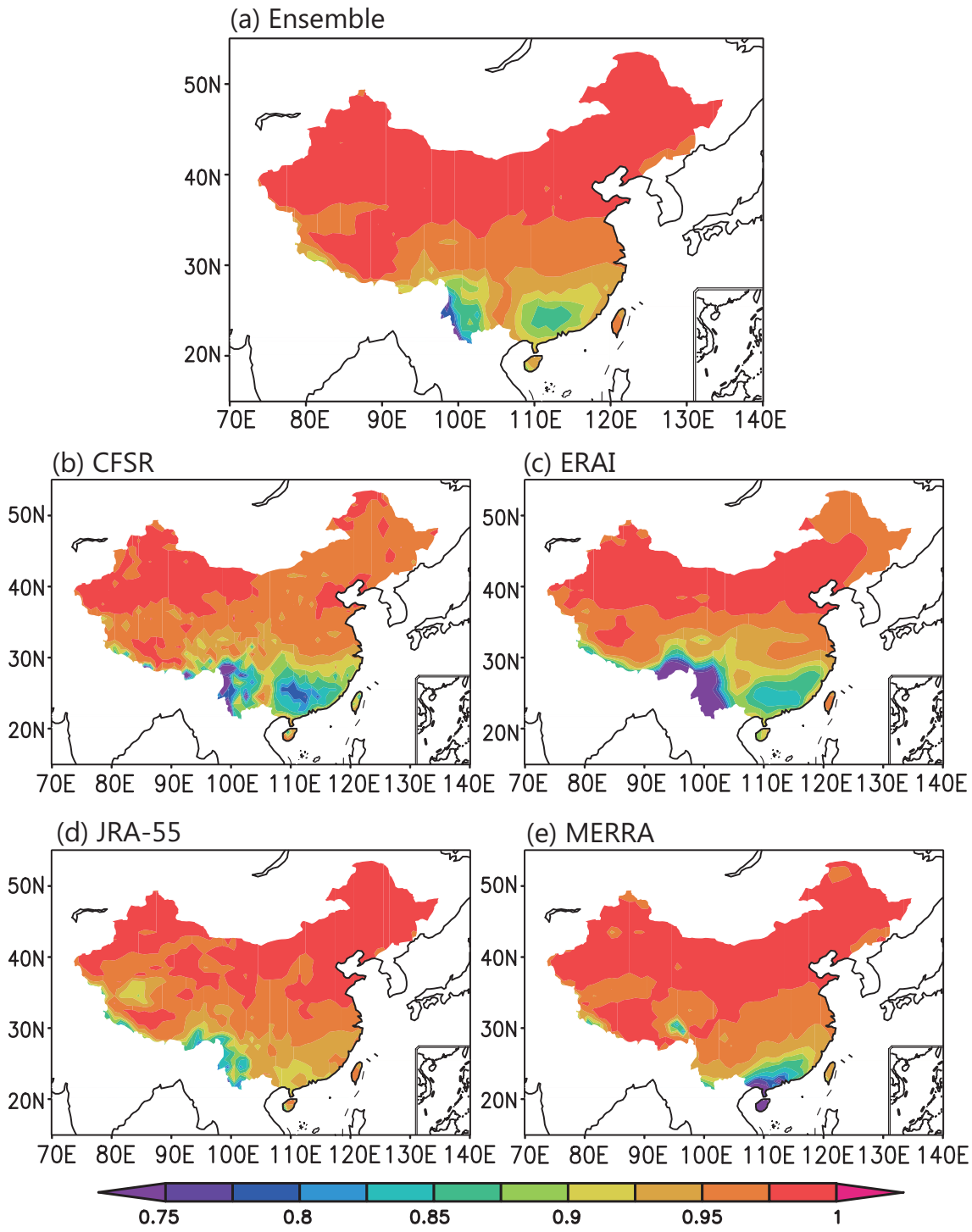

Fig. 3. Temporal correlation coefficients between CERES satellite-observed monthly net radiation and that from (a) the ensemble of the four reanalysis datasets, (b) CFSR, (c) JRA-55, (d) ERA-Interim (ERAI), and (e) MERRA, during the period from March 2000 to October 2005.

the TCCs decreased slightly over South and West China, the reanalysis products still performed well there (TCCs of 0.75–0.9). The relatively low correlation coefficients of NR between the reanalysis data and observations in southern China were attributed to the biased simulations of cloud–radiation feedback (Arakawa, 1975; Wetherald and Manabe, 1988) in the reanalysis system. Compared to southern China, with its abundant moisture and active convection, the types and variation of cloud in northern China, with its dry climate, are less complex. The models used in the reanalysis system could capture the radiation process well, via more accurate cloud–radiation feedback, in northern China.

The results of the validation suggested adequate reliability in terms of the surface energy flux obtained from the

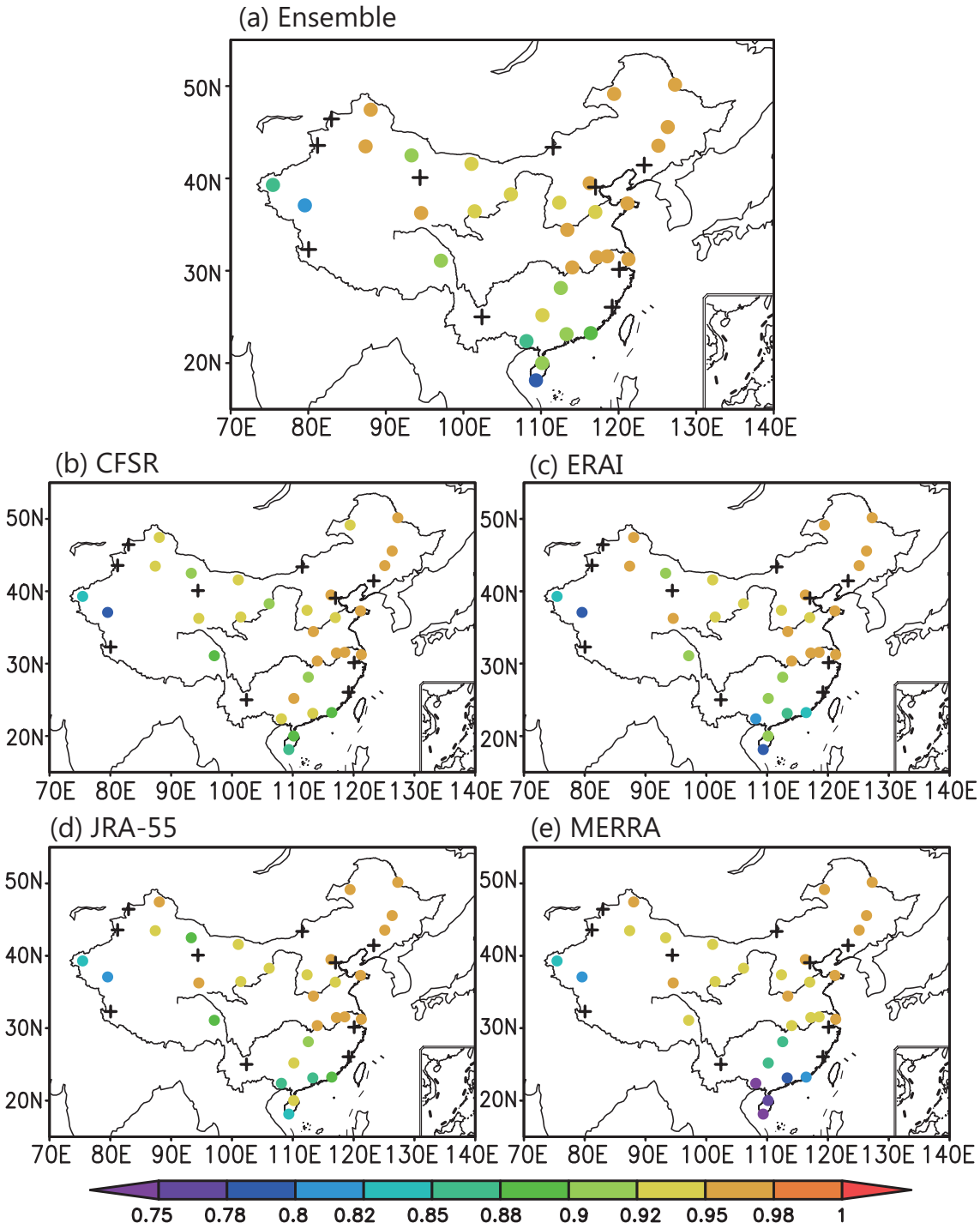

Fig. 4. Temporal correlation coefficients between measurements from radiation stations in China and the reanalysis datasets: (a) the ensemble of the four reanalysis datasets; (b) CFSR, (c) JRA-55; (d) ERA-Interim (ERAI); (e) MERRA. Colored dots indicate the correlation coefficients exceeding the 95% confidence level, and plus signs represent the correlation coefficients not exceeding the 95% confidence level.

reanalysis datasets. The four reanalysis datasets all showed high quality with respect to surface radiation, SHF and LHF. Although some uncertainty existed in the magnitude of surface turbulent fluxes (Fig. 2), we consider it minor, and not enough to alter the results of the trend analysis reported in the following section.

4. Changes in surface energy partitioning and their impacts on extreme events

To understand the variation of surface energy partitioning (or the BR) and its impacts on extreme events under a changing climate over the past three decades at the regional scale,

we first divided the study area into different climate regimes based on regional features of precipitation and temperature. The reasons why we used both temperature and precipitation (instead of precipitation only) were (1) the features of surface energy partitioning (or the BR) are closely related not only to water but also to heat, and (2) changes in BR further affect the hydrological cycle via modulating temperature and rainfall. According to the annual precipitation and temperature, as well as the topographic features (river basin and plateau), six climate regimes were considered (Fig. 5a). They included tropical monsoon regions (namely, southern China and the Yangtze River basin), with annual temperature above 15°C and rainfall amount larger than 2.5 mm d^{-1}; semi-arid and arid areas (namely, the Yellow River basin, Northeast China and Northwest China), historically prone to drought; and the high-altitude (elevation above 3000 m) and low-temperature (annual temperature below 3°C) Tibetan Plateau. The subareas defined here are similar to those used in a number of studies related to hydrological changes and drought mechanisms in China (Wang et al., 2011; Zhang and Zhou, 2015).

The distributions of climatological annual surface energy fluxes derived from the reanalysis datasets in different climate regimes are shown in Fig. 5. The downward NR ranged from 40 to 120 W m^{-2} in China and decreased with latitude (Figs. 5b–g). The radiative heating transferred largely into LHF rather than SHF over the wet monsoon areas, resulting in a relatively small BR value of below 0.6 (Figs. 5e and d). SHF (LHF) increased (decreased) with latitude in East China (east of 100°E). This caused a larger BR (0.5–1.0) in the Yellow River basin and Northeast China (Figs. 5b and c), compared to those in the southern wet regions. This result indicates that the BR tends to be large in dry regions but small in wet regions, highlighting the role of the surface wetness condition or soil moisture in surface energy partitioning (Gu et al., 2006). As for western China, the BR was greater than 1, as SHF was dominant (Figs. 5f and g). However, the BR showed a large spread among the four reanalysis products in western China.

Figure 6 shows the trends in surface energy fluxes and partitioning over the past three decades. To provide information regarding consistency and uncertainty, large (small) dots mark the regions with statistically significant trends in all four (any three among the four) of the reanalysis datasets. The annual NR displayed an upward trend over the whole of China, with an exception over the Tibetan Plateau (Fig. 6a). The maximum increase in NR, with a slope of 0.15–0.3 W m^{-2} yr^{-1}, was found in southern China. Although with a relatively small increasing trend (0.05–0.15 W m^{-2} yr^{-1}), the land surface of Northeast China also received more radiative heating from the atmosphere in recent years (Fig. 6a). Note that the NR trends over the past three decades (1979–2009) were not influenced by the data in the 1980s related to the global decrease in surface solar radiation over the 1960s–1980s (e.g., Wild, 2009). The general patterns of the NR trend in China looked similar regardless of whether or not we excluded the data in the 1980s. To further understand the dominant role

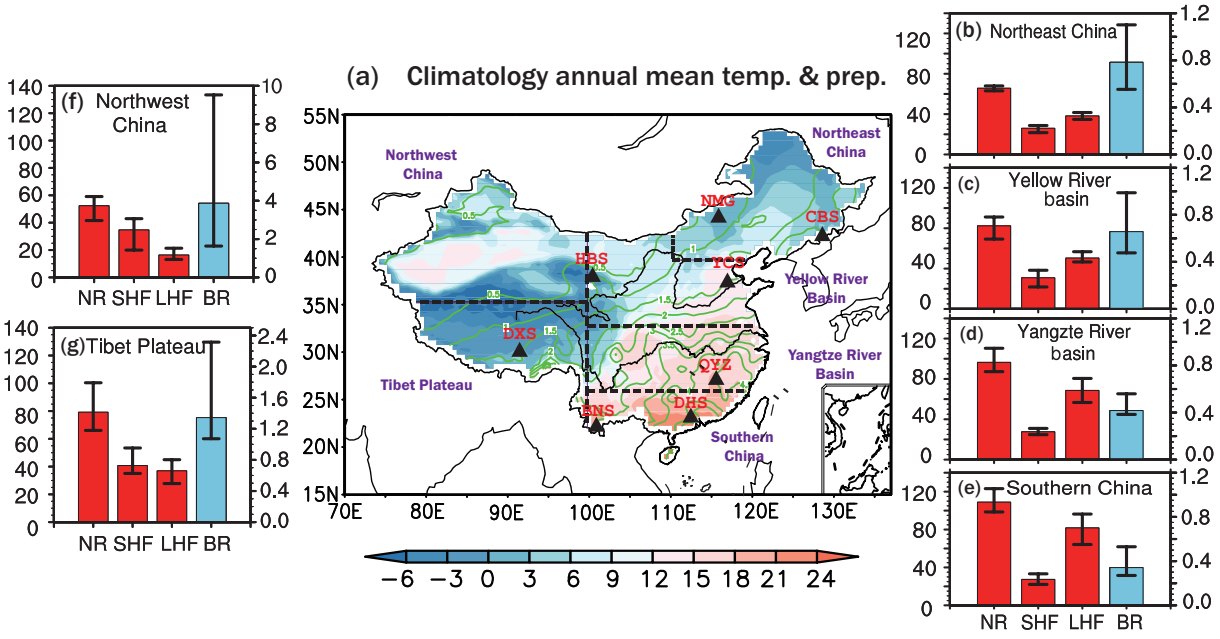

Fig. 5. (a) Distribution of climatological (1979–2009) precipitation (contours; units: mm d^{-1}) and air temperature (shading; units: °C) in China and at eight ChinaFLUX sites: BNS (22°N, 101°E); CBS (42°N, 128°E); DHS (23°N, 112°E); DXS (30°N, 91°E); HBS (38°N, 101°E); NMG (44°N, 116°E); QYZ (26°N, 115°E); YCS (36°N, 116°E). (b–g) The climatological surface net radiation (positive downwards), sensible and latent heat fluxes (positive upwards), and Bowen ratio averaged over (b) Northeast China, (c) the Yellow River basin, (d) the Yangtze River basin, (e) southern China, (f) Northwest China, and (g) the Tibetan Plateau, derived from the ensemble of the four reanalysis datasets (bars), with whiskers indicating the spread of the reanalysis datasets. Units: W m^{-2}.

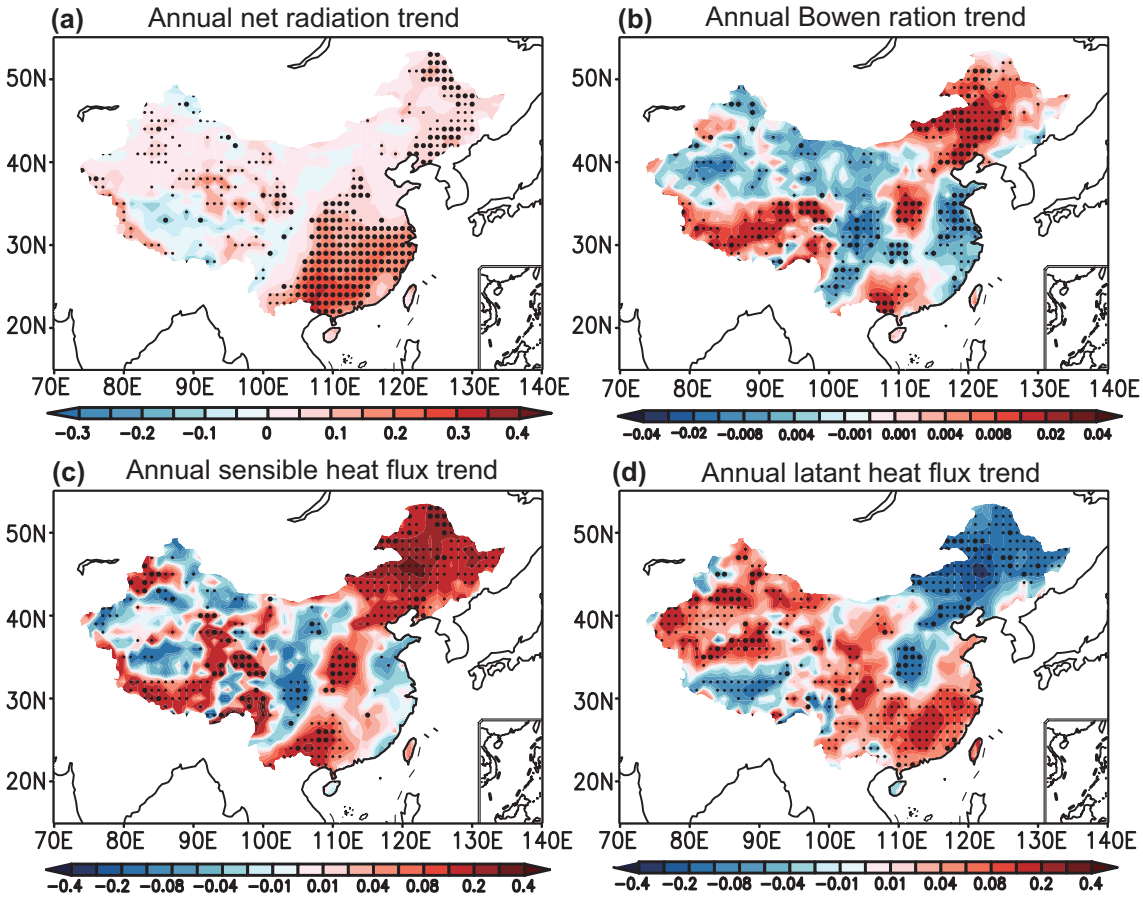

Fig. 6. Linear trends for annual-mean (a) net radiation (units: W m^{-2} yr^{-1}), (b) Bowen ratio (units: yr^{-1}), (c) sensible heat flux (units: W m^{-2} yr^{-1}), and (d) latent heat flux (units: W m^{-2} yr^{-1}). Large (small) dots denote a statistically significant trend in all four (any three among the four) of the reanalysis datasets at the 90% confidence level, based on the Mann–Kendall significant test.

in the increasing trend of annual NR observed over China with a maximum in southeastern China, the changes in the four components of NR (i.e., downward longwave/shortwave radiation and upward longwave/shortwave radiation) during the past three decades are compared in Fig. 7. We can see that the downward shortwave radiation (Fig. 7b) played the leading role in inducing the significant increase in NR over southeastern China. The upward longwave radiation (Fig. 7c) and shortwave radiation (Fig. 7d) had significant positive trends over southeastern China, while these trends were of smaller slopes compared to those of the downward shortwave radiation. The increasing trend in NR observed in Northeast China can also be attributed to increases in incident solar radiation (Fig. 7b) and longwave radiation (Figs. 7a). For western China, positive contributions of downward and upward longwave radiation (Figs. 7a and c) were partly offset by the shortwave radiation (Figs. 7b and d). In fact, China was not the only region that experienced an increased incident solar radiation over the past three decades; Wild (2009, 2012) and Wang and Dickinson (2013) documented that increased surface solar radiation occurred in many regions over the globe from the 1980s. The increased solar radiation in southern China would be associated with cloud suppression (Wild, 2012) and the slowdown in anthropogenic emissions over China (Wang and Yang, 2014).

From the perspective of surface energy balance, the change in surface radiative flux may have affected the distributions of turbulent heat fluxes. Although the NR showed a significant positive trend in East China, its effects on surface energy partitioning were diverse in different climate regimes. A significant and robust increasing (decreasing) trend of the BR was apparent in Northeast China (the Yangtze River basin), as shown in Fig. 6b. Over the monsoon regions, with their warm temperatures and abundant precipitation, the increasing trend of NR favored increasing trends in both SHF and LHF over the Yangtze River basin (Figs. 6c and d). In contrast, only SHF showed a significant increasing trend in semi-arid and arid areas, such as Northeast China (Fig. 6c), while LHF decreased there over the past three decades (Fig. 6d). These results are consistent with those in previous studies (Gu et al., 2006; Schedlbauer et al., 2011; Tang et al., 2014), which suggested that both NR and surface conditions (influenced by precipitation, near-surface air temperature, soil moisture, and vegetation, etc.) are major factors controlling the BR variability. Based on the surface flux measurements at a temperate forest site in the USA, Gu

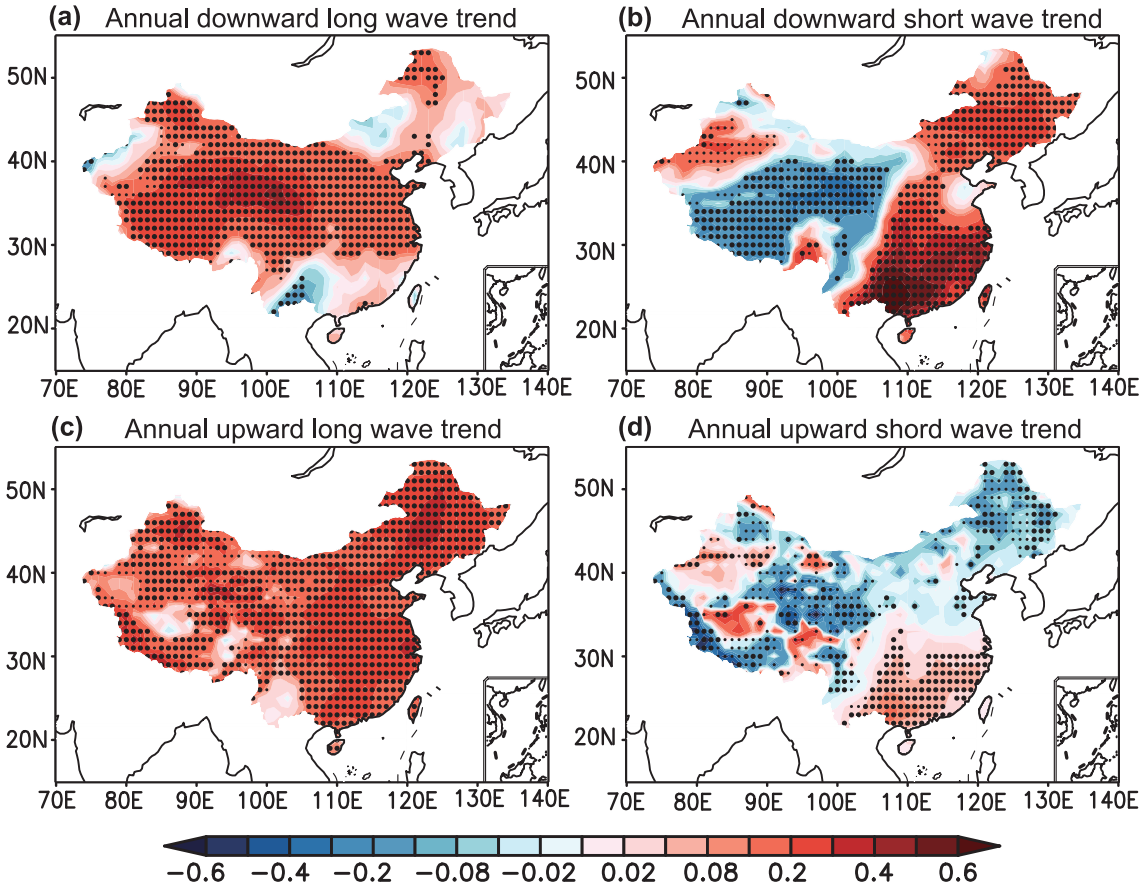

Fig. 7. Linear trends for annual-mean (a) downward longwave (units: W m^{-2} yr^{-1}), (b) downward shortwave (units: W m^{-2} yr^{-1}), (c) upward longwave (units: W m^{-2} yr^{-1}), and (d) upward shortwave (units: W m^{-2} yr^{-1}). Large (small) dots denote a statistically significant trend in all three (in any two among three) of the reanalysis datasets at the 90% confidence level, based on the Mann–Kendall significant test.

et al. (2006) found that, during the period with a nearly fixed soil moisture condition, the BR increased along with increasing NR. The increasing rate of BR given the same level of NR tended to be larger under a drought condition than under a non-drought condition. Schedlbauer et al. (2011) indicated that, in the Florida Everglades marsh area, SHF (LHF) tended to increase efficiently as NR increased under a dry (wet) surface condition, resulting in a high (low) BR value during the dry (wet) season. Tang et al. (2014) focused on the interannual variation of BR in a subtropical coniferous plantation in China. They pointed out a close connection of BR with air temperature, NR and soil moisture at the interannual timescale during the period of 2003–12.

Surface energy partitioning may describe the part of atmosphere–land interaction that influences trends in regional climate. How surface energy partitioning was influenced by and, on the other hand, exerted influences on, local climate in the Yangtze River basin and Northeast China, are illustrated in Fig. 8. Increased NR in southern China (Fig. 6a) was the key driver behind the increasing trend of LHF in the Yangtze River basin, since both local soil moisture and surface wind speed revealed downward trends (Figs. 8b and d). With its monsoon climate, the annual rainfall over the Yangtze River basin was around 3.4 mm d^{-1}, and soil moisture around 0.34 m^3 m^{-3}. Although the soil moisture tended to drop with a slight decrease in precipitation, the surface still had sufficient moisture to be evaporative. In contrast, the amount of water available in soil was limited in semi-arid areas (Fig. 8f), especially when precipitation decreased with time (Fig. 8e). Increased NR acted to heat up near-surface temperature (Fig. 8g), and the decrease in LHF or evaporation could further enhance surface warming. The upward trend in surface warming was more apparent in Northeast China (Fig. 8g) than in the Yangtze River basin (Fig. 8c). Previous studies (Zhai and Pan, 2003; Piao et al., 2010) noted that the largest warming could be found in Northeast China, where severe droughts occurred. Here, we explain the climate change in Northeast China based on the perspective of surface energy partitioning and associated land–atmosphere feedback. In summary, the long-term change of the BR associated with land–atmosphere interaction was more sensitive to climate change over the semi-arid and arid climate regimes than that over the wet climate area. In regions with a dry land condition (deficient water availability at the surface), an increasing BR occurred consistently with decreasing evaporation and soil moisture. The level of soil moisture fluctuation would then

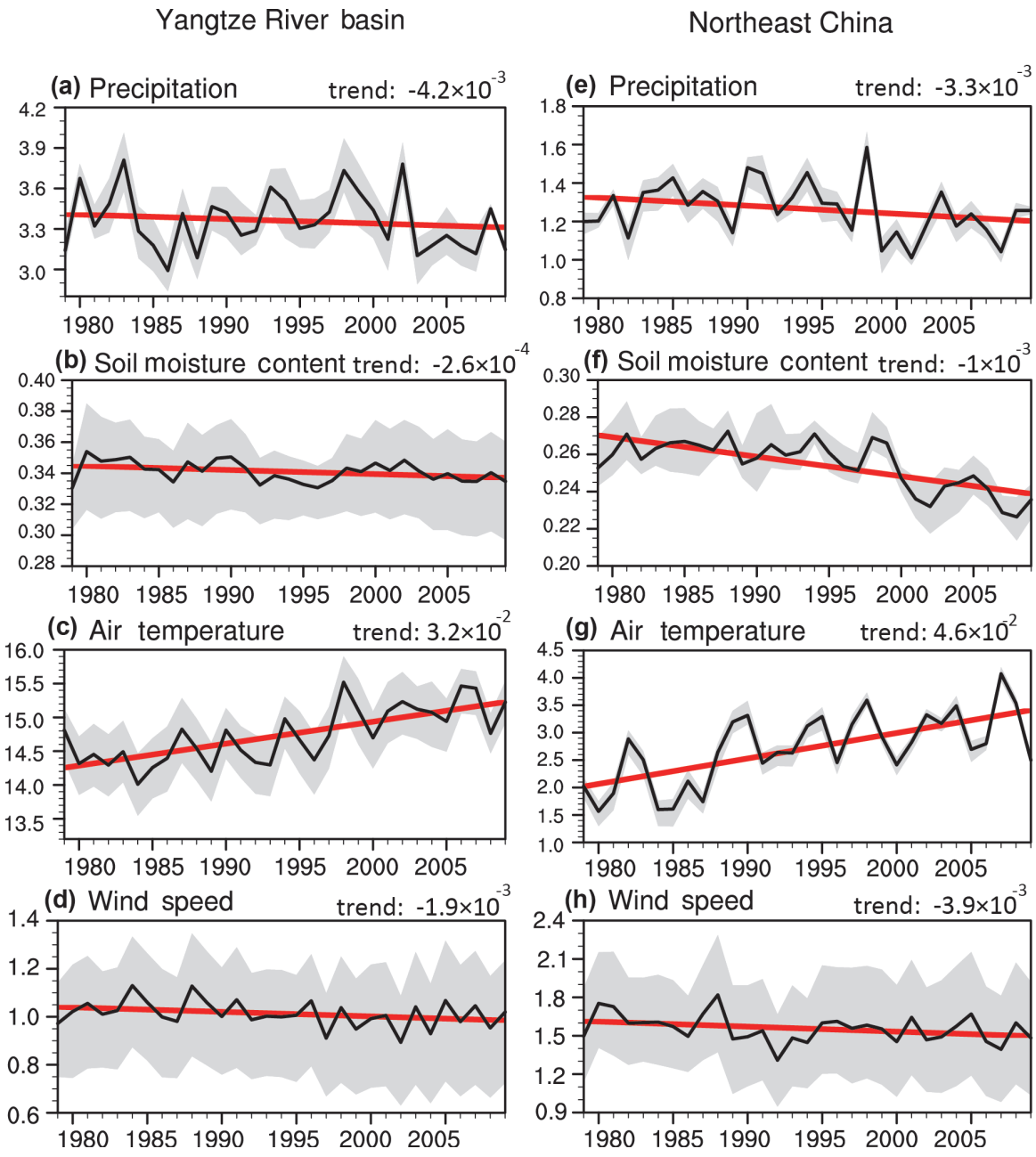

Fig. 8. Time series of annual-mean (a) precipitation (units: mm d^{-1}), (b) soil moisture (units: m^3 m^{-3}), (c) near-surface air temperature (units: °C), and (d) near-surface wind speed (units: m s^{-1}), averaged over the Yangtze River basin during 1979–2009. The average and spread of the datasets are shown by the black curve and gray shading, respectively. The linear trend over the period is indicated in red. The slope of trend is shown in the top-right of each panel. Panels (e–h) are the same as (a–d), except for the meteorological fields averaged in Northeast China.

further affect surface evaporation and temperature, causing a weakened hydrological cycle and enhanced surface warming.

The close link between surface energy partitioning and near-surface climate change (Fig. 8) suggests a possible application of the characteristics of the BR in drought monitoring. Figure 9 illustrates the distributions of standardized BR (referred to as BR index) during three major drought events. For comparison, the operational drought indices (CI and MCI) developed by the NCC are also shown. Overall, the geographical patterns of BR index, CI and MCI were highly consistent. The spatial correlation coefficients between BR index and CI/MCI were all above 0.9 for the three drought cases. The BR index also showed its capability in capturing the levels of drought severity. The maximum centers (i.e., regions suffering the most severe drought) identified by the BR index were similar to those revealed by the operational drought indices of the NCC. It is worth mentioning that, during the first drought event (left-hand panels), anomalous BR values (Fig. 9a) appeared in southern China, while this feature was absent in the CI (Fig. 9d) and MCI (Fig.

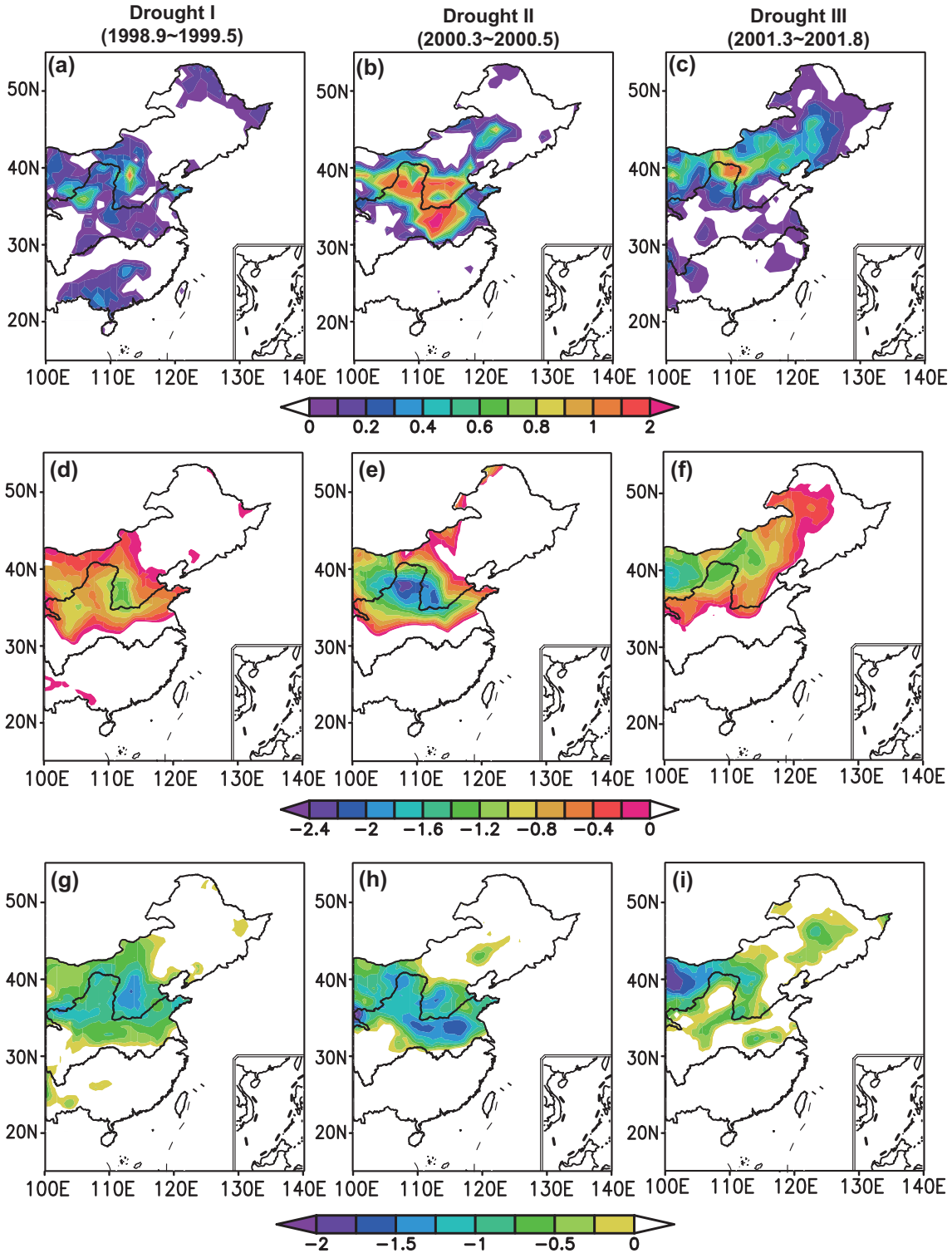

Fig. 9. Anomalies of the BR for the three major drought events in China (a) from September 1998 to May 1999, (b) from March to May 2000, and (c) from March to August 2001. Panels (d–f) and (g–i) are the same as (a–c), except for the distributions of the CI and MCI, respectively.

9g). This might be due to the definition of the MI, based on the climatological relative moisture state rather than on its anomalous or standardized quantities. In this case, the MI was larger in southern China (climatologically wet region) than in northern China (climatologically dry region), causing an increased CI/MCI in southern China even under a local drought condition. To confirm our inference, we calculated the CI/MCI based on a standardized MI. Negative CI/MCI values in southern China appeared, consistent with the distribution of BR index (not shown).

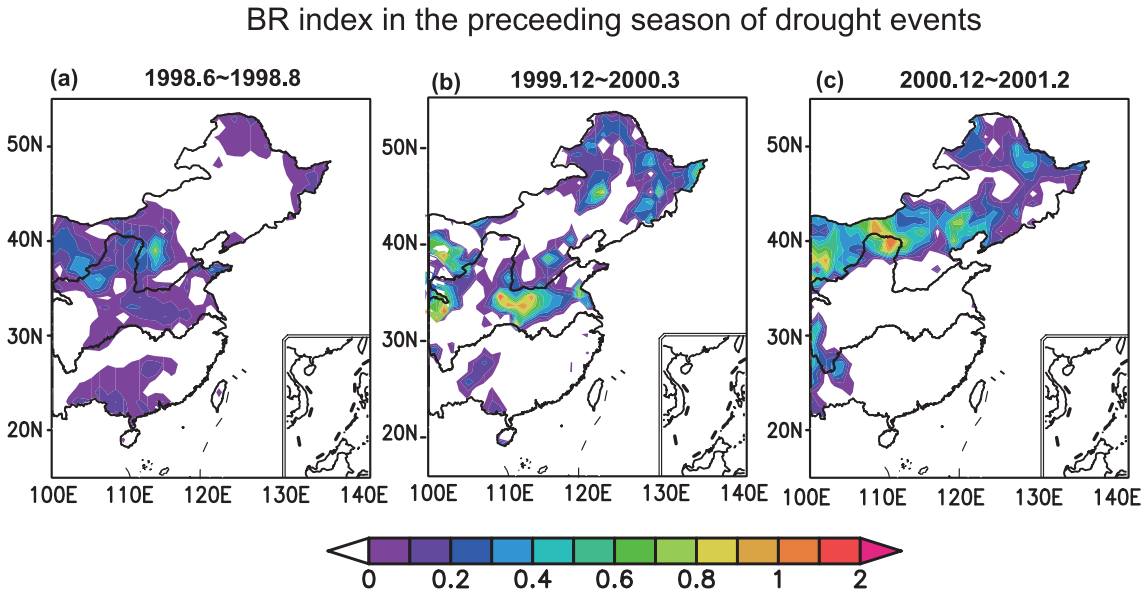

Fig. 10. Anomalies of the BR (a) from June 1998 to August 1999, (b) from December 1999 to March 2000, and (c) from December 2000 to February 2001, which are the periods of a specific season directly before each of the three drought events shown in Fig. 9.

To examine if the normalized BR index is also useful for drought prediction, the BR patterns in the preceding season (three months in advance) of drought occurrence were examined (Fig. 10). The precursor signals of a positive BR anomaly appeared over the regions where an extreme drought event was observed in the following season (Figs. 9 a–c). This suggests that BR information can be applied not only to drought monitoring but also in the early warning of severe drought events.

5. Conclusions

Land surface energy balance is a critical process of land–atmosphere exchange. NR indicates the amount of heat that can transfer from the land surface to the atmosphere via sensible and latent heating processes. The changes in the partitioning through SHF and LHF affect the surface energy balance, which in turn affects local climate, as well as hydrological and biogeochemical cycling (Shukla and Mintz, 1982; Chapin et al., 2002). Owing to the paucity of surface eddy-covariance measurements, previous studies focused mostly on short-term (such as seasonal cycle or interannual variability) changes in surface energy partitioning (or the BR) at a given location (Schedlbauer et al., 2011; Tang et al., 2014). To understand the changes in surface energy partitioning over recent decades at a continental scale, we analyzed surface energy fluxes from four modern reanalysis datasets (CFSR, ERAI, MERRA, and JRA-55). Given that the four reanalysis systems have different model physics, parameterizations and resolutions, consistent signals shown among the four (or three of the four) may represent a robust change with higher confidence. Our major findings are summarized as follows.

The state-of-the-art reanalysis products were found to represent the amplitude and variation of surface energy fluxes reasonably well. The TCCs of the NR between the reanalysis dataset and observations all exceeded 0.9 in the study domain (Figs. 3 and 4). LHF and SHF also showed high correlation (0.60–0.99; Fig. 2), providing confidence in using the reanalysis products for further analysis. Although the reanalysis datasets were found to slightly underestimate the two turbulent fluxes and overestimate the NR, the biases in amplitude were considered not to alter the results of the trend analysis in this study.

Over the past three decades (1979–2009), the annual-mean NR showed an increasing trend over the whole of China, with a maximum over southern China. This indicates that the land surface had more energy to drive heat and water exchanges. The increased available radiative flux, however, was balanced by different partitioning between SHF and LHF associated with local climate conditions. In monsoon regions, with their abundant rainfall and soil moisture (e.g., the Yangtze River basin), a remarkable upward trend in LHF could be seen, along with increased NR. Part of the increased NR was transferred to heat up the surface via SHF. However, the increasing trend in SHF was not as significant as that in LHF statistically. A decreasing trend in the BR was apparent over the Yangtze River basin (Fig. 6).

In semi-arid areas, such as Northeast China, a severe deficiency in available water at the surface led to a significant downward trend in LHF over recent decades. The increase in NR was transferred largely into SHF and raising temperature. This led to a significant increasing trend in the BR over Northeast China (Fig. 6). The combined effect of reduced LHF (or surface evaporation) and increased SHF likely contributed to the frequent number of heat extremes and drought events observed in Northeast China in recent decades (Zhai

and Pan, 2003; Piao et al., 2010).

Although it is a simple index, the BR involves information on surface heat and moisture conditions that reflect regional hydrology and climate states. Because of the similarity found between the operational CI/MCI drought index and the BR distribution during major drought events, we suggest there is potential for the BR to be used in drought monitoring. The BR index showed precursor signals in the season before the occurrence of drought, indicating its potential for the early warning of drought. Given that surface fluxes are influenced by land surface conditions, including natural (vertical gradients of temperature and moisture content, near-surface wind speed, planetary boundary layer status, and so on) and human-induced (urban heat island, land use change, agriculture and social activities) changes, the BR contains wide ranging information on heat and drought conditions, as compared to other meteorological and agricultural drought indices. Previous studies have demonstrated how human impacts (in terms of land use and land cover changes) modify Earth's surface albedo and surface–atmosphere energy exchanges, which in turn affects convective rainfall and regional climate (Otterman, 1974; Pielke, 2001; Pitman, 2003; Pielke et al., 2007). Thus, the BR might reflect different features of drought occurring across various land use and land cover types. The application of the BR in monitoring and predicting drought events is worthy of study.

Acknowledgements. We thank the anonymous reviewers for their insightful comments and suggestions. This work was supported by the Natural Science Foundation (NSF) of Jiangsu Province, China (Grant No. BK20140046) and the NSF of China (Grant No. 41375100).

REFERENCES

Arakawa, A., 1975: Modelling clouds and cloud processes for use in climate model. The physical basis of climate and climate modelling. GARP Publication Series No. 16, ICSU/WMO, 181–197.

Boer, G. J., 1993: Climate change and the regulation of the surface moisture and energy budgets. *Climate Dyn.*, **8**, 225–239.

Bosilovich, M. G., F. R. Robertson, and J. Chen, 2011: Global Energy and Water Budgets in MERRA. *J. Climate*, **24**, 5721–5739.

Bounoua, L., R. Defries, G. J. Collatz, P. Sellers, and H. Khan, 2002: Effects of land cover conversion on surface climate. *Climate Change*, **52**, 29–64.

Chapin, F. S. III, P. A. Matson, and H. A. Mooney, 2002: *Principles of Terrestrial Ecosystem Ecology*. Springer, New York, 529 pp.

Chen, B., W. C. Chao, and X. Liu, 2003: Enhanced climatic warming in the Tibetan Plateau due to doubling CO_2: A model study. *Climate Dyn.*, **20**, 401–413.

Collatz, G. J., L. Bounoua, S. O. Los, D. A. Randall, I. Y. Fung, and P. J. Sellers, 2000: A mechanism for the influence of vegetation on the response of the diurnal temperature range to changing climate. *Geophys. Res. Lett.*, **27**, 3381–3384.

Dee, D. P., and Coauthors, 2011: The ERA-Interim reanalysis: Configuration and performance of the data assimilation system. *Quart. J. Roy. Meteor. Soc.*, **137**, 553–597, doi: 10.1002/qj.828.

Defries, R. S., L. Bounoua, and G. J. Collatz, 2002: Human modification of the landscape and surface climate in the next fifty years. *Global Change Biology*, **8**, 438–458.

Ek, M. B., K. E. Mitchell, Y. Lin, E. Rogers, P. Grunmann, V. Koren, G. Gayno, and J. D. Tarpley, 2003: Implementation of Noah land surface model advances in the National Centers for Environmental Prediction operational mesoscale Eta model. *J. Geophys. Res.*, **108**, 8851, doi: 10.1029/2002JD003296.

Gu, L. H., and Coauthors, 2006: Direct and indirect effects of atmospheric conditions and soil moisture on surface energy partitioning revealed by a prolonged drought at a temperate forest site. *J. Geophys. Res.*, **111**, doi: 10.1029/2006JD007161.

Jiménez, C., and Coauthors, 2011: Global intercomparison of 12 land surface heat flux estimates. *J. Geophys. Res.*, **116**, D02102, doi: 10.1029/2010JD014545.

Keenan, T. F., D. Y. Hollinger, G. Bohrer, D. Dragoni, J. W. Munger, H. P. Schmid, and A. D. Richardson, 2013: Increase in forest water-use efficiency as atmospheric carbon dioxide concentrations rise. *Nature*, **499**, 324–327.

Kendall, M. G., 1975: *Rank Correlation Methods*. 4th ed., Charles Griffin, London.

Kobayashi, S., and Coauthors, 2015: The JRA-55 reanalysis: General specifications and basic characteristics. *J. Meteor. Soc. Japan*, **93**, 5–48, doi: 10.2151/jmsj.2015-001.

Lamarque, J. F., and Coauthors, 2013: The Atmospheric Chemistry and Climate Model Intercomparison Project (ACCMIP): Overview and description of models, simulations and climate diagnostics. *Geoscientific Model Development*, **6**, 179–206.

Liepert, B. G., 2002: Observed reductions of surface solar radiation at sites in the United States and worldwide from 1961 to 1990. *Geophys. Res. Lett.*, **29**, 61-1–61-4.

Liu, M., H. L. He, G. R. Yu, Y. Q. Luo, X. M. Sun, and H. M. Wang, 2009: Uncertainty analysis of CO_2 flux components in subtropical evergreen coniferous plantation. *Science in China Series D*: *Earth Sciences*, **52**, 257–268.

Mann, H. B., 1945: Non-parametric tests against trend. *Econometrica*, **13**, 245–259.

McKee, T. B., N. J. Doesken, and J. Kleist, 1993: The relationship of drought frequency and duration to time scales. *Proc. 8th Conf. on Applied Climatology*, Anaheim, CA, Amer. Meteor. Soc., 179–184.

Mitchell, T. D., and P. D. Jones, 2005: An improved method of constructing a database of monthly climate observations and associated high-resolution grids. *International Journal of Climatology*, **25**, 693–712.

Otterman, J., 1974: Baring high-albedo soils by overgrazing: A hypothesized desertification mechanism. *Science*, **186**, 531–533.

Piao, S. L., and Coauthors, 2010: The impacts of climate change on water resources and agriculture in China. *Nature*, **467**, 43–51.

Pielke, R. A. Sr., 2001: Influence of the spatial distribution of vegetation and soils on the prediction of cumulus convective rainfall. *Rev. Geophys.*, **39**, 151–177.

Pielke, R. A. Sr., and Coauthors, 2007: Unresolved issues with the assessment of multidecadal global land surface temperature trends. *J. Geophys. Res.*, **112**, D24S08, doi: 10.1029/2006JD008229.

Pinker, R. T., B. Zhang, and E. G. Dutton, 2005: Do satellites detect trends in surface solar radiation. *Science*, **308**, 850–854.

Pitman, A. J., 2003: The evolution of, and revolution in, land surface schemes designed for climate models. *International Journal of Climatology*, **23**, 479–510.

Richardson, A. D., T. F. Keenan, M. Migliavacca, Y. Ryu, O. Sonnentag, and M. Toomey, 2013: Climate change, phenology, and phenological control of vegetation feedbacks to the climate system. *Agricultural and Forest Meteorology*, **169**, 156–173.

Rienecker, M. R., and Coauthors, 2011: MERRA: NASA's modern-era retrospective analysis for research and applications. *J. Climate*, **24**, 3624–3648.

Schedlbauer, J. L., S. F. Oberbauer, G. Starr, and K. L. Jimenez, 2011: Controls on sensible heat and latent energy fluxes from a short-hydroperiod Florida Everglades marsh. *J. Hydrol.*, **411**, 331–341.

Shi, Q., and S. Liang, 2014: Surface-sensible and latent heat fluxes over the Tibetan Plateau from ground measurements, reanalysis, and satellite data. *Atmospheric Chemistry and Physics*, **14**, 5659–5677.

Shukla, J., and Y. Mintz, 1982: Influence of land-surface evapotranspiration on the Earth's climate. *Science*, **215**, 1498–1501.

Stanhill, G., and S. Cohen, 2001: Global dimming: A review of the evidence for a widespread and significant reduction in global radiation with a discussion of its probable causes and possible agricultural consequences. *Agricultural and Forest Meteorology*, **107**, 255–278.

Tanaka, K., H. Ishikawa., T. Hayashi, I. Tamagawa, and Y. M. Ma, 2001: Surface energy budget at Amdo on the Tibetan plateau using GAME/Tibet IOP98 data. *J. Meteor. Soc. Japan*, **79**, 505–517.

Tang, Y. K., X. F. Wen, X. M. Sun, and H. M. Wang, 2014: Interannual variation of the Bowen ratio in a subtropical coniferous plantation in southeast China, 2003–2012. *PLoS One*, **9**, e88267, doi: 10.1371/journal.pone.0088267.

Viterbo, P., and A. C. M. Beljaars, 1995: An improved land surface parameterization scheme in the ECMWF model and its Validation. *J. Climate*, **8**, 2716–2748.

Wang, A. H., D. P. Lettenmaier, and J. Sheffield, 2011: Soil moisture drought in China, 1950–2006. *J. Climate*, **24**, 3257–3271.

Wang, K. C., and R. E. Dickinson, 2013: Contribution of solar radiation to decadal temperature variability over land. *Proceedings of the National Academy of Sciences of the United States of America*, **110**, 14 877–14 882.

Wang, Y. W., and Y. H. Yang, 2014: China's dimming and brightening: Evidence, causes and hydrological implications. *Annales Geophysicae*, **32**, 41–55.

Wetherald, R. T., and S. Manabe, 1988: Cloud feedback processes in a general circulation model. *J. Atmos. Sci.*, **45**, 1397–1415.

Wielicki, B. A., B. R. Barkstrom, E. F. Harrison, R. B. Lee, and J. E. Cooper, 1996: Clouds and the earth's radiant energy system (CERES): An earth observing system experiment. *Bull. Amer. Meteor. Soc.*, **77**, 853–868.

Wild, M., 2009: Global dimming and brightening: A review. *J. Geophys. Res.*, **114**, D00D16.

Wild, M., 2012: Enlightening global dimming and brighterning. *Bull. Amer. Meteor. Soc.*, **93**, 27–37.

Wild, M., A. Ohmura, H. Gilgen, and D. Rosenfeld, 2004: On the consistency of trends in radiation and temperature records and implications for the global hydrological cycle. *Geophys. Res. Lett.*, **31**, L11201, doi: 10.1029/2003GL019188.

Wild, M., and Coauthors, 2005: From dimming to brightening: Decadal changes in solar radiation at earth's surface. *Science*, **308**, 847–850.

Wu, J., and X. J. Gao, 2013: A gridded daily observation dataset over China region and comparison with the other datasets. *Chinese Journal of Geophysics*, **56**, 1102–1111, doi: 10.6038/cjg20130406. (in Chinese with English abstract)

Yatagai, A., K. Kamiguchi, O. Arakawa, A. Hamada, N. Yasutomi, and A. Kitoh, 2012: APHRODITE: Constructing a long-term daily gridded precipitation dataset for Asia based on a dense network of rain gauges. *Bull. Amer. Meteor. Soc.*, **93**, 1401–1415.

Yu, G. R., X. F. Wen, X. M. Sun, B. D. Tanner, X. H. Lee, and J. Y. Chen, 2006: Overview of ChinaFLUX and evaluation of its eddy covariance measurement. *Agricultural and Forest Meteorology*, **137**, 125–137.

Zhai, P. M., and X. H. Pan, 2003: Change in extreme temperature and precipitation over northern China during the second half of the 20th century. *Acta Geographica Sinica*, **58**, 1–10. (in Chinese with English abstract)

Zhang, L. X., and T. J. Zhou, 2015: Drought over East Asia: A review. *J. Climate*, **28**, 3375–3399.

Zhang, Q., X. K. Zou, and F. J. Xiao, 2006: *GB/T20481-2006 Classification of meteorological drought category*. Standards Press, Beijing, China. (in Chinese)

Zou, X. K., and Q. Zhang, 2008: Preliminary studies on variations in droughts over China during past 50 years. *Journal of Applied Meteorological Science*, **19**, 679–687. (in Chinese)